analytical chemistry

pubs.acs.org/ac Article

Electrochemical Self-Sacrificial Label Conversion Coupled with DNA Framework Nanomachine Mediated Serotonin Sensing with Highly Minimized Background Noise

Baoting Dou, Yan Chen, Qiumei Feng, Huanyu Cheng, and Po Wang*

Cite This: *Anal. Chem.* 2025, 97, 157−165 Read Online

ACCESS | Metrics & More | Article Recommendations | Supporting Information

ABSTRACT: Conventional solid/liquid electrochemical interfaces typically encounter challenges with impeded mass transport for poor electrochemical quantification due to the intricate pathways of reactants from the bulk solution. To address this issue, this work reports an innovative approach integrating a target-activated DNA framework nanomachine with electrochemically driven metal−organic framework (MOF) conversion for self-sacrificial biosensing. The presence of the target biomarker serotonin initiates the DNA framework nanomachine by an entropy-driven circuit to form a cross-linked nanostructure and subsequently release the Fe-MOF probe. Acting as a natural metal precursor and a nanoconfined source of reactant, the Fe-MOF probe is converted into electroactive Prussian Blue during electrochemical processes. Taking advantage of the confinement effect, our proposed biosensor exhibits the excellent capability to detect serotonin in a linear range from 1 pM to 5 μM with a remarkable detection limit of 0.4 pM and exceptional specificity against other interferents. The proof-of-concept demonstration of serotonin detection in clinical serum samples from patients with carcinoid tumors highlights the utility of a complex sample analysis. The design could be applied for other biomarker detection with a high potential to inspire innovative sensing approaches, holding promise for applications in biomedical research and disease diagnosis.

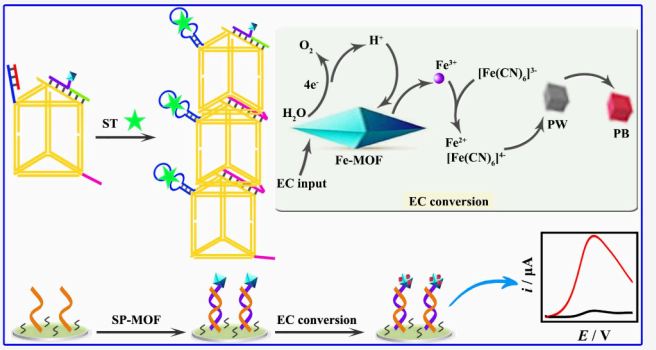

INTRODUCTION

Serotonin (ST), also known as 5-hydroxytryptamine, plays a pivotal role as a signaling molecule influencing human emotions and behaviors.[1,2] Acting as a neurotransmitter in the brain, it regulates various biological systems as a peripheral hormone.[3] Dysregulation of ST levels is linked to various disease conditions such as depression,[4] addiction,[5] and carcinoid tumors.[6] Therefore, the determination of ST amounts is crucial for disease prevention and clinical diagnosis. Conventional methods for measuring ST rely on its redox activity, chemical structure, or optical properties, including electrochemical analysis,[7] mass spectrometry,[8] fluorescent analysis,[9] and so on. Among these, electrochemical sensors offer advantages such as high sensitivity, rapid response, affordability, ease of use, and miniaturization. Additionally, there has been a surge in the development of molecular probes capable of detecting and responding to ST by various covalent or noncovalent interactions, such as aptamers,[10,11] genetically encoded proteins,[12,13] and organic molecules.[14] Aptamers, synthetic oligonucleotides derived from *in vitro* selection experiments, offer benefits such as high affinity, selectivity, and ease of synthesis.[15−17] In comparison, genetically encoded proteins require genetic manipulation, while organic molecules come with concerns regarding selectivity.[17] Consequently, an aptameric electrochemical sensor represents an efficient tool for monitoring ST levels.

Driven by the entropic gain of the liberated molecules, the entropy-driven circuit is a convenient and stable amplification circuit.[18,19] Since the groundbreaking study in 2007,[19] entropy-driven DNA circuits have found extensive applications in molecule detection, logic analysis, and nanostructure assembly. This wide application is attributed to their remarkable catalytic efficiency, signal amplification, and customizable networks.[20−22] For example, intracellular entropy-driven multivalent DNA circuits leverage target biomarkers to initiate signal amplification processes, allowing for multibit computing to differentiate cancer cell types and track tumor advancement.[23] Compared with alternative enzyme-free amplification techniques, the entropy-driven module adeptly prevents circuit leakage, leading to decreased noise levels and enhanced reliability. However, the canonical entropy-driven circuit

Received: July 4, 2024
Revised: October 9, 2024
Accepted: November 3, 2024
Published: January 2, 2025

Scheme 1. Schematic Diagram of a Target-Activated DNA Framework Nanomachine Coupled with Electrochemical Self-Sacrificial Label Conversion for Signal Amplification to Detect Serotonin of Ultralow Concentration

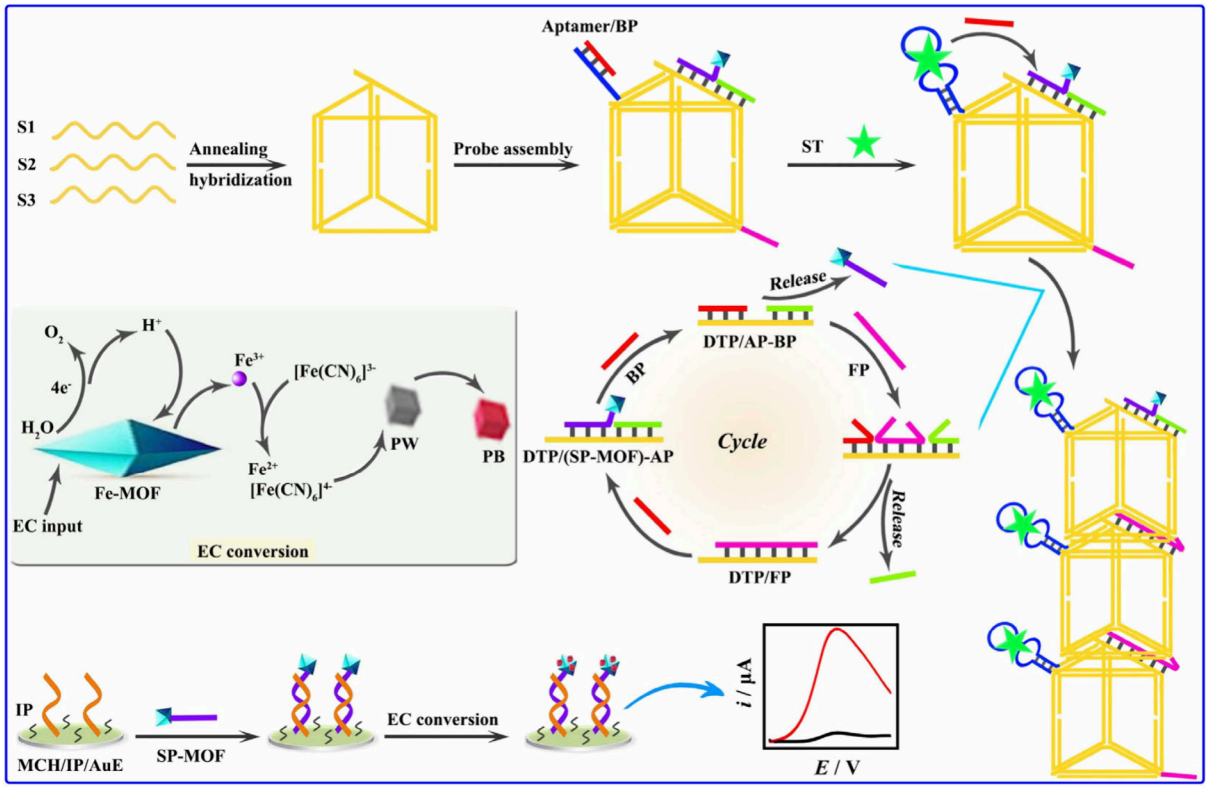

consists of several freely diffusible components in solution, thus severely lowering the reaction speed and efficiency due to the molecular proximity effect.[24,25] The DNA nanoarchitecture fabricated by DNA components could confine reactants within a compact space,[26−28] which increases the local concentrations of DNA reagents to exert a spatial-confinement effect, resulting in steerable dynamic operations and exhibiting a higher signal-to-noise ratio. Therefore, a DNA framework nanomachine (e.g., 3D DNA triangular prism) functionalized with the reagents of an entropy-driven circuit is expected to yield an efficient electrochemical platform.

The mass transport at the sensing interface significantly impacts the detection performance of the sensor. Impeded electrochemical quantification often results from complex transportation pathways and reactant dilution in a large volume of bulk solution.[29−31] By introducing reactants or precursors onto the sensing interface, a confinement effect can be generated on the reactants near the electrodes,[32,33] presenting a facile avenue for manipulating mass transport near the sensing interface. Metal−organic frameworks (MOFs)[34−37] are widely acknowledged for their abundant metal elements, customizable functional groups, superior biocompatibility, and other advantageous properties. Therefore, it is of high interest to combine MOFs as templated reactant sources with suitable signal detection technologies to mitigate the mass transportation issue in bulk solution.

This work presents an innovative electrochemical sensing strategy that combines electrochemical self-sacrificial label conversion employing a MOF substrate nanomaterial with a DNA framework nanomachine for signal detection. The proposed sensing strategy offers three key advantages. First, the abundant metal elements in the MOF can be converted to generate amplified sensing signals, eliminating the need for additional reactants. Second, entropy-driven DNA circuit reactants fixed on the 3D DNA framework can significantly enhance reaction efficiency and reduce background signals. Lastly, effective signal amplification and minimal background noise can lead to a low detection limit in human serum, showing promise for the sensitive detection of various biomarkers directly relevant to the diagnostic confirmation of varying disease conditions.

EXPERIMENTAL SECTION

The Preparation of SP-MOF. The Fe-MOF was synthesized via a hydrothermal route. Initially, Pluronic F127 (0.16 g) was dissolved in the deionized water (11 mL) and then mixed with 4 mL of 200 mM $FeCl_3$ solution. Subsequently, 75 μL of CH_3COOH was added to the mixture and stirred for 1 h, followed by the addition of 60 mg of 2-aminoterephthalic acid (NH_2-BDC) with stirring for 2 h. The resulting solution was then transferred to a stainless-steel-lined Teflon autoclave and heated to 110 °C for 24 h. The Fe-MOF product was obtained after three rounds of centrifugation and washing with ethanol. Additionally, a mixture of Fe-MOF (1 mL, 1 mg/mL), signal probe (SP, 100 μL, 1 μM), 40 mM *N*-ethyl-*N*′-(3-(dimethylamino)propyl)carbodiimide hydrochloride (EDC), and 10 mM *N*-hydroxysuccinimide (NHS) was stirred for 5 h, and the precipitate was collected by centrifugation to yield SP-MOF.

The Fabrication of MCH/IP/AuE. The gold electrode (AuE, 3 mm) was pretreated by immersion in a freshly prepared piranha solution (98% H_2SO_4 and 30% H_2O_2 at a volume ratio of 3:1) for 30 min. Subsequently, the electrode was thoroughly rinsed with water, polished with a 0.3 and 0.05

https://doi.org/10.1021/acs.analchem.4c03452
Anal. Chem. 2025, 97, 157−165

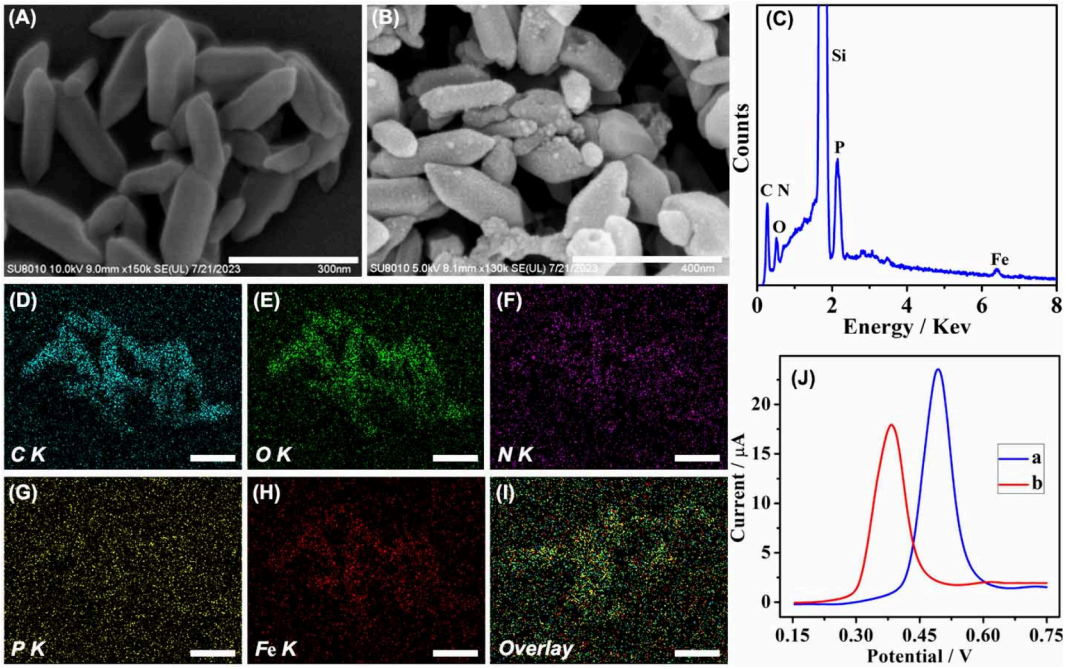

Figure 1. SEM of Fe-MOFs before (A) and after (B) EC conversion. Scale bar: 300 and 400 nm for parts A and B. (C) EDS profile of the Fe-MOF probe after EC conversion. EDS mapping of (D) C, (E) O, (F) N, (G) P, (H) Fe, and (I) overlays in the Fe-MOF probe after EC conversion. Scale bar: 1 μm. (J) Differential pulse voltammetry (DPV) responses in 0.1 M K_2SO_4 solution containing (a) 100 mM $FeCl_3$ and (b) 100 mM $K_3[Fe(CN)_6]$.

μm aluminum slurry for 5 min each, and then sonicated in pure water, ethanol, and pure water for 5 min each to remove any residual alumina powder. Following this, each AuE underwent electrochemical cleaning in 0.5 M H_2SO_4, with potential scanning from 0.3 to 1.5 V until stable characteristic voltammetric peaks occurred. Subsequently, a mixed solution of immobilization probe (IP, 0.6 μM) and tris(2-carboxyethyl)phosphine hydrochloride (TCEP, 10 mM) was allowed to react for 60 min to reduce the disulfide bond and then transferred to the cleaned AuE overnight. Finally, 6-mercapto-1-hexanol (MCH, 1 mM) was cast onto the sensing interface for 1 h to block it.

The Detection Procedure of ST. The DNA triangular prism (DTP) structure was prepared by mixing the S1, S2, and S3 in equal quantities, followed by annealing hybridization in 20 mM Tris-HCl buffer (2 mM EDTA, 12.5 mM $MgCl_2$, pH 7.4), which was heated to 95 °C for 5 min and then slowly cooled to room temperature. Next, the DTP structure was hybridized with aptamer/blocking probe (BP), SP-MOF, assistance probe (AP), S1D, S3U, and S3D at room temperature for 2 h, further mixed with fuel probe (FP) at the same molar ratio, and incubated at room temperature for another 2 h. When the sensor was applied for the quantitative determination of ST, DTP/(aptamer/BP+(SP-MOF)-AP+FP) (600 nM) was reacted with different concentrations of ST on the electrode for 30 min. After the SP-MOF was introduced on the sensing interface, the sensor underwent electrochemical conversion in a solution containing 0.5 mM $K_3[Fe(CN)_6]$ and 0.1 M K_2SO_4, followed by a potential of 1.6 V scanned for 600 s and a potential of 0 V scanned for 300 s, with a sample interval of 0.002 s.

Clinical Sample Analysis. Sera from patients with carcinoid tumors and healthy volunteers were obtained from the affiliated hospital of Xuzhou Medical University (Jiangsu, China). All participants provided informed consent prior to the study. The collection and handling of samples adhered to the World Health Organization (WHO) guidelines for blood collection (WHO Publication ISBN-13:978-92-4-159922-1, 2010) and were approved by the Ethics Committee of the affiliated hospital of Xuzhou Medical University. Prior to analysis, red blood cells (RBCs) were isolated from the blood samples by centrifugation at 7500g for 10 min, and other proteins or tissues were removed using Amicon Ultra-05 centrifugal Ultracel-10 membrane filter tubes. Subsequently, the serum samples were either mixed with DTP/(aptamer/BP+(SP-MOF)-AP+FP) for electrochemical detection or reacted with reagents from an enzyme-linked immunosorbent assay (ELISA) kit for colorimetric detection.

RESULTS AND DISCUSSION

Mechanism of the Electrochemical Self-Sacrificial Label Conversion Sensing. The programmable DNA framework nanomachine is constructed following the design strategy shown in Scheme 1. The DTP basic structure is obtained through the annealed hybridization of three single-stranded DNA molecules (S1, S2, and S3) with similar lengths (Figures S1, S2). Three modules of aptamer/BP, SP-MOF, AP, and FP could be self-assembled on the DTP structure, in which aptamer/BP and FP are located at opposite vertices of the triangular prism. The three-stranded hybridization complex DTP/(SP-MOF)-AP along the opposite edge of the triangular prism could act as an entropy-driven module. The association of ST with the aptamer probes leads to a conformational change in the pseudoknot aptamer structure and releases the BP strand, which could activate the entropy-driven strand displacement reaction. In this reaction, BP first combines with the terminal toehold to displace the SP-MOF probe, resulting in exposure of the new toehold at the middle domain of the DTP opposite edge. The FP strand on the middle toehold

https://doi.org/10.1021/acs.analchem.4c03452
Anal. Chem. 2025, 97, 157−165

further results in the second strand displacement reaction to cause the release of BP and AP from the DTP complex. The released BP would react with the next DTP to initiate the cascade strand displacement reaction. Accompanying the entropy-driven strand displacement reaction, the adjacent DTP complexes would self-assemble with each other to form the cross-linked nanostructure. On the other hand, a large number of SP-MOF released during the cascade reaction would be hybridized with IP and loaded on the electrode. Ultimately, the modified MOF probes serve as porous metal precursors for electrochemical conversion (EC), facilitating the production of electroactive Prussian Blue (PB) and consequently amplifying the signal for ST detection. The conversion mechanism is succinctly outlined as follows: EC input with a high potential applied to the electrode initiates the water-splitting reaction, leading to the production of H^+ ions on the sensing interface. The presence of H^+ establishes an acidic microenvironment, facilitating the dissociation of the MOFs to release Fe^{3+}. Subsequently, Fe^{3+} and $[Fe(CN)_6]^{3-}$ undergo electrochemical reduction to form Fe^{2+} and $[Fe(CN)_6]^{4-}$ at a low applied potential. The reaction between Fe^{2+} and $[Fe(CN)_6]^{4-}$ results in the formation of Prussian White (PW), which is then oxidized by O_2, leading to the generation of PB. The detailed reactions are elucidated as follows.

$$2H_2O \rightarrow 4H^+ + O_2 + 4e^- \quad (1)$$

$$Fe - MOF \xrightarrow{H^+} Fe^{3+} \quad (2)$$

$$Fe^{3+} + [Fe(CN)_6]^{3-} + 2e^- \rightarrow Fe^{2+} + [Fe(CN)_6]^{4-} \quad (3)$$

$$Fe^{2+} + [Fe(CN)_6]^{4-} + 2K^+ \rightarrow K_2Fe[Fe(CN)_6](PW) \quad (4)$$

$$K_2Fe[Fe(CN)_6](PW) \xrightarrow{O_2/H_2O} KFe[Fe(CN)_6](PB) + K^+ + e^- \quad (5)$$

Characterizations of the Fe-MOF Conversion. The scanning electron microscopy (SEM) image in Figure 1A shows the characteristic polyhedral morphology of the prepared Fe-MOFs, with an average size of approximately 300 nm. Electrochemical conversion changes the crystal structures of Fe-MOFs due to the *in situ* production of cubic PB on the surface of Fe-MOFs (Figure 1B). Investigation of the constitution of the Fe-MOF probe with energy-dispersive X-ray spectrometry (EDS) indicated the existence of C, N, O, Fe, and P elements (Figure 1C). The elemental mappings in Figures 1D–I suggest a homogeneous distribution of these elements throughout the Fe-MOF. As evidenced by the presence of the P element, the DNA probes are loaded on the Fe-MOFs. By applying the electrochemical method, the reduction process of Fe^{3+} and $[Fe(CN)_6]^{3-}$ is examined to understand the generation mechanism of PB. The reduction of Fe^{3+} to Fe^{2+} begins below 0.6 V, whereas the reduction of $[Fe(CN)_6]^{3-}$ to $[Fe(CN)_6]^{4-}$ begins below 0.5 V (Figure 1J). As a result, only Fe^{3+} reduces to Fe^{2+} at a potential between 0.5 and 0.6 V, but the electrochemical reduction of Fe^{3+} and $[Fe(CN)_6]^{3-}$ to Fe^{2+} and $[Fe(CN)_6]^{4-}$ occurs simultaneously for a potential of less than 0.5 V. The electrochemical reduction of Fe^{2+} and $[Fe(CN)_6]^{4-}$ leads to the formation of PW, which is eventually oxidized to PB.

The cyclic voltammetry (CV) characterization of the EC conversion product PB shows remarkable redox peaks near 0.2 V for the sensor with Fe-MOF (a) compared to unobvious peaks without (b) (Figure 2A), suggesting the satisfactory

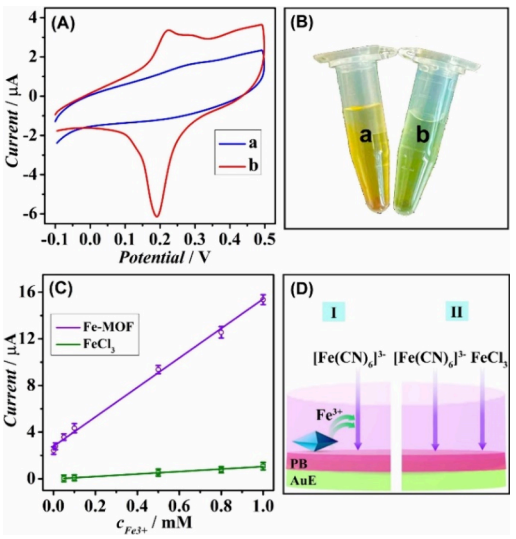

Figure 2. (A) CV responses of AuE after EC conversion in the absence (a) and presence (b) of 1 mg/mL Fe-MOF in a mixture of 0.5 mM $K_3[Fe(CN)_6]$ and 0.1 M K_2SO_4. (B) Photos of the mixture containing 1 mg/mL Fe-MOF, 0.5 mM $K_3[Fe(CN)_6]$, and 0.1 M K_2SO_4 before (a) and after (b) EC conversion. (C) The current responses of PB produced by Fe-MOF and $FeCl_3$ were under different concentrations. Error bar: standard deviation (SD); the number of measurements (n): 3. (D) The mass transport of Fe-MOF (I) and $FeCl_3$ (II) during EC conversion.

electrochemical activity of PB. In addition, the solution of Fe-MOF, $K_3[Fe(CN)_6]$, and K_2SO_4 changes from a tan to a blue color (Figure 2B) after the EC conversion, in which the gradually deepened blue color demonstrated the formation of PB, indicating that Fe-MOF is the self-sacrificial template of Fe^{3+} for PB generation. The traditional electrochemical deposition method was carried out using $FeCl_3$ under identical conditions as a comparison. Figure 2C illustrates that the current response of PB synthesized via the proposed EC strategy (Fe-MOF) significantly exceeded that of the traditional electrochemical deposition method, using $FeCl_3$. Notably, when the Fe^{3+} concentration in the conventional electrochemical deposition method was below 0.05 mM, the current responses of PB were negligible. In contrast, the EC conversion strategy displayed a significant current response even at an Fe^{3+} concentration as low as 1 μM, suggesting the high production efficiencies of PB. The superior performance could be attributed to the generation-confinement effect, where Fe^{3+} was generated *in situ* on the sensing interface and confined within a nanoliter-volume layer, leading to increased local reactant concentrations that enhance electrosynthesis. Conversely, in the traditional method, the concentration of Fe^{3+} was decreased after a transportation gradient (Figure 2D). These findings highlight the superiority of the EC conversion strategy in improving electrodeposition and quantification over the conventional approach.

The influences of EC potential and the amount of $K_3[Fe(CN)_6]$ on the sensor's responses were investigated. As shown in Figure S3A, the current response of the sensor increased gradually with the elevation of EC potential from

https://doi.org/10.1021/acs.analchem.4c03452
Anal. Chem. 2025, 97, 157−165

1.50 V to 1.60 V and leveled off thereafter. This behavior signified the attainment of equilibrium in the electrochemical conversion reaction at 1.60 V. The dependence of the current response of the sensor on the concentration of $K_3[Fe(CN)_6]$ is illustrated in Figure S3B. With the elevation of $K_3[Fe(CN)_6]$ concentration from 0.1 mM to 0.9 mM, the maximum current signal was obtained at 0.5 mM, which is the optimal concentration for sensing applications.

Characterizations of the DTP Machine. Gel electrophoresis experiments for entropy-driven strand displacement reaction and DTP assembly investigate the mechanism of the target-activated DNA framework nanomachine. The distinct bands of S2/SP-AP, FP, and aptamer/BP (lanes 1−3 in Figure 3A) indicate the high hybridization efficiency of the DNA

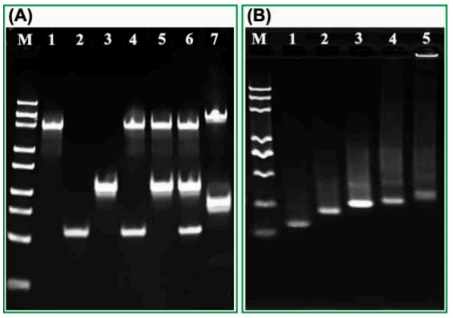

Figure 3. (A) Native polyacrylamide gel electrophoresis characterization of S2/SP-AP (1), FP (2), aptamer/BP (3), S2/SP-AP + FP (4), S2/SP-AP + aptamer/BP (5), S2/SP-AP + FP + aptamer/BP (6), and S2/SP-AP + FP + aptamer/BP + ST (7). (B) Agarose gel electrophoresis of S1 (1), S1 + S2 (2), S1 + S2 + S3 (3), DTP (4), and DTP + ST (5).

probes. The same migration velocity from the mixture of S2/SP-AP duplex and FP as the original DNA probes (lane 4) suggests that the strand displacement reaction could not be triggered by FP, because the BP strand was confined in the aptamer/BP duplex in the absence of target. An insignificant change in the DNA bands is observed when S2/SP-AP is mixed with aptamer/BP (lane 5). Similarly, the S2/SP-AP, FP, and aptamer/BP probes (lane 6) display the same migration velocity as those of the DNA bands. The lower migration velocity from the new band with added ST (lane 7) originated from the S2/FP confirms the entropy-driven strand displacement circuit initiated by target ST. Agarose gel electrophoresis evaluates the hybridization of DTP probes (Figure 3B). A clear independent and nontrailing band with lower electrophoretic mobility (lane 3) suggests the complete hybridization between these DNA strands (S1, S2, and S3) combined in equimolar quantities during the thermal annealing process. The successive hybridization with other DTP probes would further decrease the electrophoretic mobility (lane 4) due to the increase in the molecular weight, indicating the formation of the DTP nanostructure. Importantly, the DTP incubated with ST (lane 5) with a much lower electrophoretic mobility suggests an interlinked DTP structure in the presence of ST.

The structural investigation of the DNA products with atomic force microscopy (AFM) reveals a near monodisperse particle population for the DTP complex (Figure 4A). In comparison to the individual DTP, the intercrossing of polymer chains results from the strand displacement initiated by ST (Figure 4B), demonstrating the formation of multiple interlinked DTP complexes. The size of the DTP can be

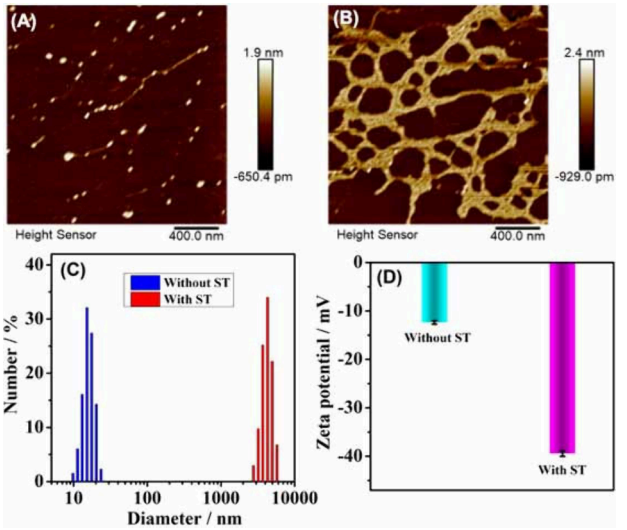

Figure 4. AFM images of DTP/(aptamer/BP+SP-AP+FP) in the (A) absence and (B) presence of ST. (C) DLS and (D) zeta potential analysis of the DTP/(aptamer/BP+SP-AP+FP) structure. Error bar: SD, $n = 3$.

estimated based on the circumcircle diameter model. With the 34-base edge (a) of DTP measured as 12 nm, the radius (r) of the circumscribed circle of the bottom face would be $r = (2/3) \times (3/2)^{1/2} \times 6.9$ nm. The distance (d) from the center of the sphere to the center of the bottom face is the same as half of the side length, which is 6 nm. By applying the Pythagorean theorem,[38−40] the value of R can be determined as $R = (6.9^2 + 6^2)^{1/2} = 9.2$ nm (Figure S4). The circumcircle diameter of the rigid DTP construction is then estimated to be $9.2 \times 2 = 18.4$ nm. A diameter range of 13.5 to 21 nm is observed in the dynamic light scattering (DLS) analysis of the DTP structure (blue, Figure 4C), which is slightly different from the estimation possibly due to the distortion of DNA nanostructures. Coincident with the AFM characterization, the diameter of the nanocomplexes expanded as a result of the intercrossing DTP nanostructures (red). The shifted zeta potential of DTP from −12.3 to −39.4 mV after the introduction of ST (Figure 4D) provides additional evidence of the association of the DTP complexes.

Characterizations of the Sensing Interface Construction. Electrochemical impedance spectroscopy (EIS) and CV measurements analyze the stepwise modification of the electrodes, substantiating the construction of this sensing interface. The EIS response fitted to a Randles equivalent circuit (inset in Figure 5A) consists of the solution resistance (R_s), electron transfer resistance (R_{et}), Warburg impedance (W), and constant phase element (Q_{dl}). The diameter of the semicircle in the Nyquist diagram reflects the R_{et} of the redox conversion of the electroactive substance $[Fe(CN)_6]^{3-/4-}$ at a specific applied potential. The bare electrode (curve a) demonstrates a low R_{et} value to suggest exceptional electrical conductivity of the AuE (Figure 5A). A significant increase in R_{et} after the IP and MCH mixed monolayer self-assembled on the electrode (curve b) is primarily attributed to the repulsion of $[Fe(CN)_6]^{3-/4-}$ from AuE due to the negative charges on the phosphate backbone of IP. Incubation of MCH/IP/AuE with DTP/(aptamer/BP+SP-AP+FP) gives a negligible increase in R_{et} (curve c), suggesting that the SP is unable to hybridize with IP in the absence of ST. The significant increase

https://doi.org/10.1021/acs.analchem.4c03452
Anal. Chem. 2025, 97, 157−165

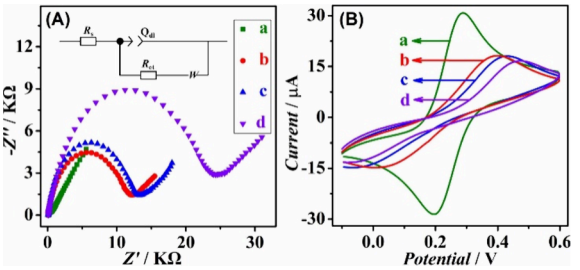

Figure 5. (A) EIS and (B) CV characterizations of the sensor in 1 mM $[Fe(CN)_6]^{3-/4-}$ solution containing 0.1 M KCl: (a) bare AuE, (b) MCH/IP/AuE, (c) MCH/IP/AuE incubated with DTP/(aptamer/BP+SP-AP+FP) in the absence of ST, and (d) MCH/IP/AuE incubated with DTP/(aptamer/BP+SP-AP+FP) in the presence of ST. The DC potential, frequency range, and amplitude applied for EIS experiments were 0.24 V, 10^5−0.1 Hz, and 5 mV, respectively.

in R_{et} upon the addition of ST (curve d) primarily comes from the hybridization of SP on the electrode caused by ST. The CV responses (Figure 5B) reveal a pair of clear redox peaks in the bare electrode (curve a) and decreased peak currents upon successful fixation of IP and MCH on the electrode (curve b). The presence of ST (curve d) results in a noticeably larger response than that in the absence of ST (curve c). Consistent results from both CV and EIS characterizations confirm the successful fabrication of the biosensor.

Feasibility for the Amplified Detection of ST. The feasibility of the designed approach for ST detection is examined by performing DPV tests on different modified AuE surfaces (Figure 6). Due to the lack of PB signal in the buffer,

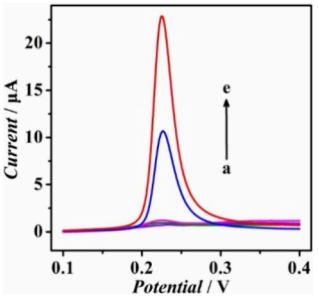

Figure 6. DPV responses of the sensing electrode incubated with the different solutions: (a) DTP/(aptamer/BP + SP-AP + FP); (b) DTP/(aptamer/BP + SP-AP + FP) and ST; (c) DTP/(aptamer/BP + (SP-MOF)-AP + FP); (d) DTP/(aptamer/BP + (SP-MOF)-AP) and ST; and (e) DTP/(aptamer/BP + (SP-MOF)-AP + FP) and ST.

the sensing electrode does not exhibit any peak current (curve a) when incubated with DTP/(aptamer/BP+SP-AP+FP). Similarly, when the sensor is incubated with DTP/(aptamer/BP+SP-AP+FP) and the target ST, there is hardly any change in the current (curve b). In the absence of ST, the electrode surface based on DTP/(aptamer/BP+(SP-MOF)-AP+FP) exhibits a low current response, as seen from curve c, suggesting the nonspecific adsorption of a small amount of PB. The sensor exposed to the mixture of ST and DTP/(aptamer/BP+(SP-MOF)-AP) without FP results in a distinct peak at approximately 0.23 V (curve d), indicating the electrochemical reduction of the surface-confined PB. Additionally, the introduction of FP induces a substantial increase in current response (curve e), which is attributed to the significantly attached PBs onto the sensor surface via a cascade strand displacement reaction. These results thus provide clear evidence of remarkable signal amplification from the proposed method.

Optimization of the Detection Conditions. To improve the sensitivity of the sensor, some key experimental parameters were optimized, including the concentration of IP, the reaction temperature, and the reaction time. As shown in Figure 7A,

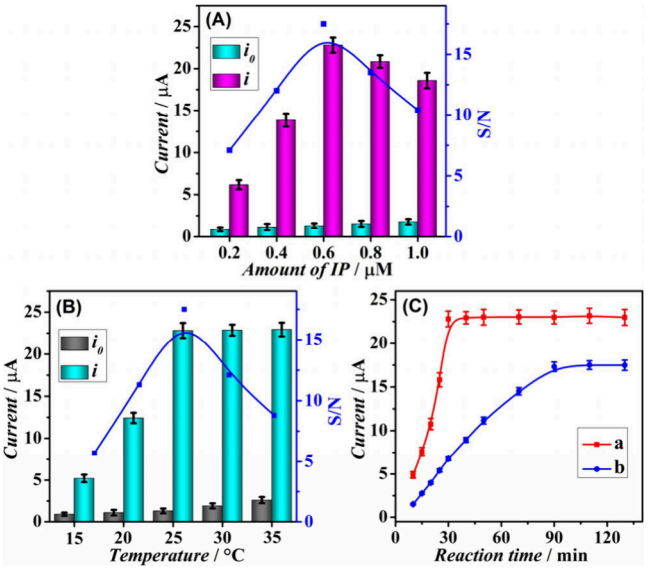

Figure 7. (A) The relationship between the current responses and the concentration of IP was assessed with a reaction temperature of 25 °C and a reaction time of 110 min. (B) The current responses of the sensor at different reaction temperatures with the IP concentration of 0.6 μM and a reaction time of 110 min. (C) The effect of reaction time on the current responses of the DTP machine (a) and the traditional DNA machine (b) with an IP concentration of 0.6 μM and a reaction temperature of 25 °C. Error bar: SD, n = 3.

with the IP concentration increased from 0.2 to 1.0 μM, the background current response increased gradually, whereas the signal current response to ST increased from 0.2 to 0.6 μM and decreased between 0.6 and 1.0 μM, indicating the steric hindrance and diminished efficiency of the DNA reaction from the high IP concentration. To achieve the highest signal-to-noise ratio (represented by S/N = i/i_0, where i and i_0 are the DPV currents in the presence and absence of ST), an IP concentration of 0.6 μM was selected for the following studies. The effect of reaction temperature on the sensor's response was investigated in Figure 7B. With the gradual increase in reaction temperature from 15 to 25 °C, a corresponding rise in current response was observed in the presence of ST, which was attributed to the enhanced reactivity of the entropy-driven DNA machine at higher temperature. However, the higher temperature (>25 °C) resulted in increased background response and a false-positive rate, ultimately causing a decrease in the signal-to-noise ratio. Consequently, the optimal signal-to-noise ratio was reached at 25 °C for ST detection. Moreover, the effect of reaction time on the current responses of the DTP machine and the traditional DNA machine is contrastively studied in Figure 7C. The traditional DNA machine followed the same design as the DTP machine but used entropy-driven DNA circuit components in the bulk solution (in contrast to the DTP structure). It was demonstrated that the current response of the DTP machine

https://doi.org/10.1021/acs.analchem.4c03452
Anal. Chem. 2025, 97, 157−165

initially increased with the reaction time and reached a plateau of 22.8 μA at 30 min (curve a), which was much larger and faster than the traditional DNA machine (17.3 μA at 90 min, curve b). The advancement of reaction speed and detection efficiency was attributed to the confinement effect and the improved mass transport.

Detection Performances and Real Samples' Analysis. As shown in Figure 8A, under the optimal experimental conditions, the DPV current of the sensor increased gradually with the increase in ST concentration from 1 pM to 5 μM. The linear relationship between the current and the logarithm of ST concentration was obtained as i = 5.446 log c + 66.95 (R^2 = 0.9957) (Figure 8B), and the limit of detection (LOD) was calculated to be 0.4 pM according to the formula LOD = $3S_b/m$, where S_b signifies the standard deviation of the blank tests and m stands for the slope of the calibration curve in the linear region.[41−43] As a result, the biosensor from this work exhibited superior analytical capabilities when compared to the other reported detection methods based on fluorescence, phosphorescence, or liquid chromatography (Table S1), possibly attributed to the efficient signal amplification and the reduced noise. To demonstrate the reproducibility of the sensing system, the parallel detection of ST was performed with six sensors prepared independently, and the DPV responses of six different electrodes displayed a relative standard deviation (RSD) of 3.9% following incubation with 10 nM ST under identical experimental conditions, confirming excellent reproducibility of the approach.

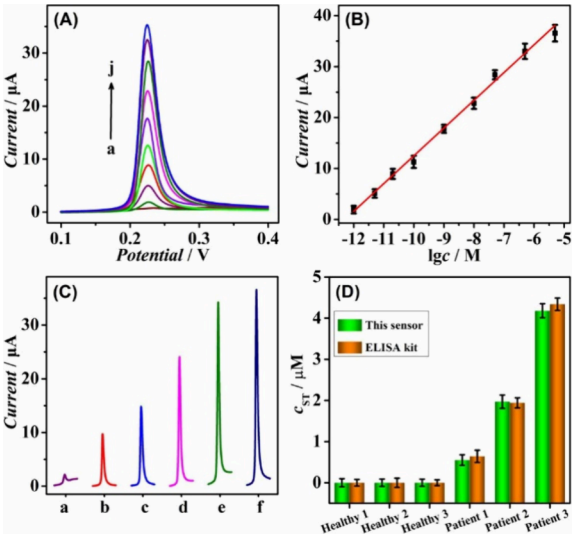

Figure 8. (A) DPV responses of ST at various concentrations in buffer, from a to j: 0 pM, 1 pM, 5 pM, 20 pM, 100 pM, 1 nM, 10 nM, 50 nM, 500 nM, 5 μM. (B) The calibration curve of the current vs the logarithm of ST concentration in buffer. (C) DPV responses of the sensor to ST in the human serum samples, from a to f: 1 pM, 20 pM, 100 pM, 10 nM, 500 nM, 5 μM. (D) Analysis of ST in different clinical samples. Error bar: SD, n = 3.

The specificity of the proposed strategy is showcased by detecting endogenous molecules in complex biological environments (e.g., ST metabolites with common neurotransmitters). The incubation of norepinephrine (NE), glycine (Gly), tryptophan (Trp), glucose (Glu), histamine (His), or 5-methoxy tryptophan (MTP) (concentration of 200 nM) with the sensing probes produces minimal current changes compared with the blank response in the absence of ST (Figure S5). In contrast, the addition of ST (10 nM) even at a 20-fold lower concentration than the interferents results in a significantly higher current response. Furthermore, the mixture of ST and the control molecules (Mix) yields a current signal similar to that of ST alone. These findings indicate that the developed method exhibits excellent selectivity for the target ST due to the highly specific binding between ST and the aptamer sequence.

The long-term stability of the sensor was assessed by the successive detection of 10 nM ST following storage at 4 °C for various durations. It was found that the signal decline of the sensor was less than 2% of the initial current within 5 days. Subsequently, the current responses of the sensor were obtained to be 97.3%, 96.4%, and 95.5% of the original signal after storage of 10, 20, and 30 days, respectively, revealing satisfactory stability of the sensor for continuous operation.

The application of the proposed method in complex biological samples first starts with the evaluation using healthy human serum samples spiked with different concentrations of ST (1, 20, 100, 10, 500, and 5 μM). The presence of target ST leads to significantly increased current in DPV responses with the rising ST concentration (curves a to f in Figure 8C). A strong linear relationship between the current and the logarithm of ST concentration is also observed: i = 5.381 log c + 67.38, as evidenced by a high coefficient of determination (R^2 = 0.9962, Figure S6A). The potential of the developed sensor is further highlighted in a proof-of-concept demonstration to detect ST in clinical serum samples from patients with carcinoid tumors. Based on the linear calibration curve, the ST concentrations in the serum samples from three carcinoid tumor patients are measured to be 0.55, 1.97, and 4.18 μM, which are higher than those in healthy serum samples (Figure 8D). The rise of ST levels in serum samples of carcinoid tumor patients, compared to those of healthy volunteers, is consistent with previous research.[44−46] The accuracy of the established sensing system is validated by analyzing the identical clinical serum samples with a commercially available serotonin ELISA kit (Abcam, ab133053) that shows a linear dependence as Abs = −0.1330 log c − 0.7016 (R^2 = 0.9775) (Figure S6B). The detection results of the proposed sensor were compared with the standard ELISA kit using the Student t-test, which demonstrated an acceptable statistical variance of 0.4% at the 95% confidence level, confirming the accuracy of the sensor for the assay of complex biological samples.

CONCLUSIONS

In conclusion, a highly effective and robust electrochemical sensing platform is established for the sensitive detection of serotonin with an ultralow detection limit. This system introduces an innovative electrochemical self-sacrificial label conversion strategy utilizing an Fe-MOF probe as the metal precursor. In conjunction with a target-activated DNA framework nanomachine, the developed sensor demonstrates remarkable sensitivity for serotonin detection within a highly linear range along with an ultralow detection limit of 0.4 pM within 1 h. Moreover, the successful detection of serotonin in serum samples from healthy and irradiated patients underscores its potential for practical applications. When the appropriate affinity pairs are incorporated, the sensing approach presented here can be expanded to detect a more diverse set of biomarkers. This advancement is poised to

https://doi.org/10.1021/acs.analchem.4c03452
Anal. Chem. 2025, 97, 157−165

stimulate novel methodologies in the design and application of electrochemical platforms for biomolecular sensing and disease diagnoses.

■ ASSOCIATED CONTENT

Supporting Information

The Supporting Information is available free of charge at https://pubs.acs.org/doi/10.1021/acs.analchem.4c03452.

Chemicals and materials; native polyacrylamide gel electrophoresis analysis; agarose gel analysis; ELISA experiment for ST determination; electrochemical, AFM, and SEM measurements; supplementary figures; supplementary table; and supplementary references (PDF)

■ AUTHOR INFORMATION

Corresponding Author

Po Wang − *School of Chemistry and Materials Science, Jiangsu Normal University, Xuzhou, Jiangsu 221116, China;* orcid.org/0000-0001-6590-2169; Email: wangpo@jsnu.edu.cn

Authors

Baoting Dou − *School of Chemistry and Materials Science, Jiangsu Normal University, Xuzhou, Jiangsu 221116, China*

Yan Chen − *School of Chemistry and Materials Science, Jiangsu Normal University, Xuzhou, Jiangsu 221116, China*

Qiumei Feng − *School of Chemistry and Materials Science, Jiangsu Normal University, Xuzhou, Jiangsu 221116, China;* orcid.org/0000-0002-6576-6811

Huanyu Cheng − *Department of Engineering Science and Mechanics, Pennsylvania State University, State College, Pennsylvania 16802, United States;* orcid.org/0000-0001-6075-4208

Complete contact information is available at: https://pubs.acs.org/10.1021/acs.analchem.4c03452

Author Contributions

All authors have given approval to the final version of the manuscript.

Notes

The authors declare no competing financial interest.

■ ACKNOWLEDGMENTS

This work was supported by the National Natural Science Foundation of China (21675067 and 22404067), the Natural Science Foundation of Jiangsu Province (BK20210917 and BE2019645), the Natural Science Foundation of Xuzhou City (KC23238), the Priority Academic Program Development (PAPD) of Jiangsu Higher Education Institutions, and the Six Talent Peak Project in Jiangsu Province for distinguished scholars (2019-SWYY-084). H.C. acknowledges the support provided by NSF (Grant No. 2309323) and Penn State University.

■ REFERENCES

(1) Dinarvand, M.; Neubert, E.; Meyer, D.; Selvaggio, G.; Mann, F. A.; Erpenbeck, L.; Kruss, S. *Nano Lett.* **2019**, *19*, 6604−6611.

(2) Liu, Y.; Jiang, Y.; Si, Y.; Kim, J. Y.; Chen, Z. F.; Rao, Y. *Nature* **2011**, *472*, 95−99.

(3) Li, Y.; Zhong, W.; Wang, D.; Feng, Q.; Liu, Z.; Zhou, J.; Jia, C.; Hu, F.; Zeng, J.; Guo, Q.; Fu, L.; Luo, M. *Nat. Commun.* **2016**, *7*, 10503.

(4) Wan, J.; Peng, W.; Li, X.; Qian, T.; Song, K.; Zeng, J.; Deng, F.; Hao, S.; Feng, J.; Zhang, P.; Zhang, Y.; Zou, J.; Pan, S.; Shin, M.; Venton, B. J.; Zhu, J. J.; Jing, M.; Xu, M.; Li, Y. *Nat. Neurosci.* **2021**, *24*, 746−752.

(5) Li, Y.; Simmler, L. D.; Van Zessen, R.; Flakowski, J.; Wan, J.; Deng, F.; Li, Y.; Nautiyal, K. M.; Pascoli, V.; Lüscher, C. *Science* **2021**, *373*, 1252−1256.

(6) Valentino, J. D.; Li, J.; Zaytseva, Y. Y.; Mustain, W. C.; Elliott, V. A.; Kim, J. T.; Harris, J. W.; Campbell, K.; Weiss, H.; Wang, C.; et al. *Clin. Cancer Res.* **2014**, *20*, 1212−1222.

(7) Sasa, S.; Blank, C.; Wenke, D. C.; Sczupak, C. *Clin. Chem.* **1978**, *24*, 1509−1514.

(8) Dale, G. L.; Friese, P.; Batar, P.; Hamilton, S. F.; Reed, G. L.; Jackson, K. W.; Clemetson, K. J.; Alberio, L. *Nature* **2002**, *415*, 175−179.

(9) Zhao, C.; Cheung, K. M.; Huang, I. W.; Yang, H.; Nakatsuka, N.; Liu, W.; Cao, Y.; Man, T.; Weiss, P. S.; Monbouquette, H. G.; Andrews, A. M. *Sci. Adv.* **2021**, *7*, No. eabj7422.

(10) Stuber, A.; Douaki, A.; Hengsteler, J.; Buckingham, D.; Momotenko, D.; Garoli, D.; Nakatsuka, N. *ACS Nano* **2023**, *17*, 19168−19179.

(11) Nakatsuka, N.; Yang, K. A.; Abendroth, J. M.; Cheung, K. M.; Xu, X.; Yang, H.; Zhao, C.; Zhu, B.; Rim, Y. S.; Yang, Y.; et al. *Science* **2018**, *362*, 319−324.

(12) Pedelacq, J. D.; Cabantous, S.; Tran, T.; Terwilliger, T. C.; Waldo, G. S. *Nat. Biotechnol.* **2006**, *24*, 79−88.

(13) Kubitschke, M.; Müller, M.; Wallhorn, L.; Pulin, M.; Mittag, M.; Pollok, S.; Ziebarth, T.; Bremshey, S.; Gerdey, J.; Claussen, K. C.; et al. *Nat. Commun.* **2022**, *13*, 7525.

(14) Mei, Y.; Zhang, Q. W.; Gu, Q.; Liu, Z.; He, X.; Tian, Y. *J. Am. Chem. Soc.* **2022**, *144*, 2351−2359.

(15) Victorious, A.; Zhang, Z.; Chang, D.; Maclachlan, R.; Pandey, R.; Xia, J.; Gu, J.; Hoare, T.; Soleymani, L.; Li, Y. *Angew. Chem., Int. Ed.* **2022**, *61*, No. e202204252.

(16) Zou, Z.; Pan, M.; Mo, F.; Jiang, Q.; Feng, A.; Zhou, Y.; Wang, F.; Liu, X. *Chem. Sci.* **2022**, *13*, 12198−12207.

(17) Song, G.; Zou, Z.; Feng, A.; Li, C.; Liang, M.; Wang, F.; Liu, X. *Anal. Chem.* **2023**, *95*, 9076−9082.

(18) Li, H.; Han, M.; Weng, X.; Zhang, Y.; Li, J. *ACS Nano* **2021**, *15*, 1710−1717.

(19) Zhang, D. Y.; Turberfield, A. J.; Yurke, B.; Winfree, E. *Science* **2007**, *318*, 1121−1125.

(20) Yang, S.; Luo, J.; Zhang, L.; Feng, L.; He, Y.; Gao, X.; Xie, S.; Gao, M.; Luo, D.; Chang, K. *Adv. Sci.* **2023**, *10*, 2301814.

(21) Zhang, Q.; Zhao, R.; Li, C.; Zhang, Y.; Tang, C.; Luo, X.; Ma, F.; Zhang, C. *Anal. Chem.* **2022**, *94*, 13978−13986.

(22) Zhang, C.; Wang, Z.; Liu, Y.; Yang, J.; Zhang, X.; Li, Y.; Pan, L.; Ke, Y.; Yan, H. *J. Am. Chem. Soc.* **2019**, *141*, 17189−17197.

(23) Bai, M.; Chen, F.; Cao, X.; Zhao, Y.; Xue, J.; Yu, X.; Fan, C.; Zhao, Y. *Angew. Chem., Int. Ed.* **2020**, *59*, 13267−13272.

(24) Liu, L.; Hong, F.; Liu, H.; Zhou, X.; Jiang, S.; Šulc, P.; Jiang, J.; Yan, H. *Sci. Adv.* **2022**, *8*, No. eabm9530.

(25) Chatterjee, G.; Dalchau, N.; Muscat, R. A.; Phillips, A.; Seelig, G. *Nat. Nanotechnol.* **2017**, *12*, 920−927.

(26) Ahmad, K.; Javed, A.; Lanphere, C.; Coveney, P. V.; Orlova, E. V.; Howorka, S. *Nat. Commun.* **2023**, *14*, 3630.

(27) Li, X.; Jia, Y.; Zhang, Y.; Chen, H.; Xu, J. *Chem. Sci.* **2023**, *14*, 7699−7708.

(28) Yang, L. M.; Yin, X. H.; An, B.; Li, F. *Anal. Chem.* **2021**, *93*, 1709−1716.

(29) Krabbenborg, S. O.; Huskens, J. *Angew. Chem., Int. Ed.* **2014**, *53*, 9152−9167.

(30) Wang, J.; Liu, G.; Merkoçi, A. *J. Am. Chem. Soc.* **2003**, *125*, 3214−3215.

(31) Wang, J. G.; Yu, R. J.; Hua, X.; Long, Y. T. *Chem. Soc. Rev.* **2023**, *52*, 2596−2616.

(32) Li, C.; Jiang, B.; Wang, Z.; Li, Y.; Hossain, M. S. A.; Kim, J. H.; Takei, T.; Henzie, J.; Dag, Ö.; Bando, Y.; Yamauchi, Y. *Angew. Chem., Int. Ed.* **2016**, *55*, 12746−12750.
(33) Zhang, Q.; Li, L.; Qiao, Z.; Lei, C.; Fu, Y.; Xie, Q.; Yao, S.; Li, Y.; Ying, Y. *Anal. Chem.* **2017**, *89*, 12145−12151.
(34) Xu, W.; Wu, Y.; Gu, W.; Du, D.; Lin, Y.; Zhu, C. *Chem. Soc. Rev.* **2024**, *53*, 137−162.
(35) Shi, X.; Ling, Y.; Li, Y.; Li, G.; Li, J.; Wang, L.; Min, F.; Hübner, R.; Yuan, S.; Zhan, J.; Cai, B. *Angew. Chem., Int. Ed.* **2023**, *62*, No. e202316257.
(36) Jin, K.; Moon, D.; Chen, Y. P.; Park, J. *Adv. Mater.* **2024**, *36*, 2309570.
(37) Liu, X. J.; Gao, X.; Yang, L. M.; Zhao, Y. C.; Li, F. *Anal. Chem.* **2021**, *93*, 11792−11799.
(38) Campbell, J. F.; Tessmer, I.; Thorp, H. H.; Erie, D. A. *J. Am. Chem. Soc.* **2008**, *130*, 10648−10655.
(39) Schneider, T. D. *Nucleic Acids Res.* **2010**, *38*, 5995−6006.
(40) Liu, Y.; Chen, Q.; Liu, J.; Yang, X.; Guo, Q.; Li, L.; Liu, W.; Wang, K. *Anal. Chem.* **2017**, *89*, 3590−3596.
(41) Radi, A. E.; Acero Sánchez, J. L.; Baldrich, E.; O'Sullivan, C. K. *J. Am. Chem. Soc.* **2006**, *128*, 117−124.
(42) Dou, B.; Wang, K.; Chen, Y.; Wang, P. *Anal. Chem.* **2024**, *96*, 10594−10600.
(43) Dou, B.; Zhou, H.; Han, X.; Wang, P. *Anal. Chem.* **2023**, *95*, 994−1001.
(44) Ying, X.; Chen, J.; Tu, D.; Zhuang, Y.; Wu, D.; Shen, L. *ACS Appl. Mater. Interfaces* **2021**, *13*, 6421−6429.
(45) Ko, M.; Mendecki, L.; Eagleton, A. M.; Durbin, C. G.; Stolz, R. M.; Meng, Z.; Mirica, K. A. *J. Am. Chem. Soc.* **2020**, *142*, 11717−11733.
(46) Wu, S.; Lin, Y.; Liu, J.; Shi, W.; Yang, G.; Cheng, P. *Adv. Funct. Mater.* **2018**, *28*, 1707169.

https://doi.org/10.1021/acs.analchem.4c03452
Anal. Chem. 2025, 97, 157−165